The Journal of Clinical Endocrinology & Metabolism, 2021, Vol. XX, No. XX, 1–10
doi:10.1210/clinem/dgaa964
Clinical Research Article

Clinical Research Article

Paraneoplastic Secretion of Multiple Phosphatonins From a Deep Fibrous Histiocytoma Causing Oncogenic Osteomalacia

Melvin Khee Shing Leow,[1,2,3,4,5] Shaillay Dogra,[1] Xiaojia Ge,[1] Khoon Leong Chuah,[6] Huiling Liew,[4] Kelvin Siu Hoong Loke,[7] and Craig McFarlane[1,8]

[1]Singapore Institute for Clinical Sciences (A*STAR), Brenner Centre for Molecular Medicine, Singapore; [2]Lee Kong Chian School of Medicine, Nanyang Technological University, Singapore; [3]Yong Loo Lin School of Medicine, National University of Singapore, Singapore; [4]Department of Endocrinology, Division of Medicine, Tan Tock Seng Hospital, Singapore; [5]Cardiovascular and Metabolic Disorders Program, Duke-NUS Medical School, Singapore; [6]Department of Pathology, Tan Tock Seng Hospital, Singapore; [7]Department of Nuclear Medicine and Molecular Imaging, Singapore General Hospital, Singapore; and [8]Department of Molecular & Cell Biology, College of Public Health, Medical and Veterinary Sciences, James Cook University, Townsville QLD, Australia.

ORCiD number: 0000-0002-2837-5889 (M. K. S. Leow); 0000-0002-7056-8887 (C. McFarlane).

Received: 2 November 2020; Editorial Decision: 21 December 2020; First Published Online: 19 January 2021; Corrected and Typeset: 19 January 2021.

Abstract

Context: Literature suggests that oncogenic osteomalacia is usually caused by a benign mesenchymal tumor secreting fibroblast growth factor subtype-23 (FGF-23), but the involvement of other phosphatonins has only been scarcely reported. We have previously published a seemingly typical case of oncogenic osteomalacia. Following curative neoplasm resection, we now report unique molecular characteristics and biology of this tumor.

Case Description: A 25-year-old man had been diagnosed with severe oncogenic osteomalacia that gradually crippled him over 6 years. ^{68}Ga-DOTA-TATE positron emission tomography/computed tomography scan localized the culprit tumor to his left sole, which on resection revealed a deep fibrous histiocytoma displaying a proliferation of spindle cells with storiform pattern associated with multinucleated giant cells resembling osteoclasts. Circulating FGF-23, which was elevated more than 2-fold, declined to undetectable levels 24 h after surgery. Microarray analysis revealed increased tumor gene expression of the phosphatonins FGF-23, matrix extracellular phosphoglycoprotein (MEPE) and secreted frizzled-related protein subtype 4, with elevated levels of all 3 proteins confirmed through immunoblot analysis. Differential expression of genes involved in bone formation and bone mineralization were further identified. The patient made an astonishing recovery from being wheelchair bound to fully self-ambulant 2 months postoperatively.

ISSN Print 0021-972X ISSN Online 1945-7197
Printed in USA

Conclusion: This report describes oncogenic osteomalacia due to a deep fibrous histiocytoma, which coincidentally has been found to induce profound muscle weakness via the overexpression of 3 phosphatonins, which resolved fully upon radical resection of the tumor. Additionally, genes involved in bone formation and bone remodeling contribute to the molecular signature of oncogenic osteomalacia.

Key Words: phosphatonin, oncogenic osteomalacia, hypophosphatemia, FGF-23, deep fibrous histiocytoma

Oncogenic osteomalacia is a very rare endocrine paraneoplastic syndrome typified by chronic eucalcemic hypophosphatemia, phosphaturia, and normal parathyroid hormone (PTH) due to circulating phosphatonin secreted by a tumor (1). The majority of such cases are due to paraneoplastic secretion of fibroblast growth factor subtype-23 (FGF-23) by benign mesenchymal tumors, although malignant tumors have also been described (1,2). In some instances, PTH may be elevated due to secondary hyperparathyroidism as a compensatory response to overcome the inhibitory effects of FGF-23 on 1,25-dihydroxycholecalciferol.

We have previously reported the case of a young man who was diagnosed at age 25 with oncogenic osteomalacia incapacitated and wheelchair bound by the time he presented to us (3). The tumor in the sole of his left foot, which was responsible for his severe muscle weakness, was resected, whereupon he made an astounding recovery. This is a follow-up report that describes the interesting and unique molecular and cellular features of the tumor, which corroborates with the limited data in the extant literature.

Case Report

A 25-year-old Indonesian Malay man without any medical history developed a progressive debilitating illness 6 years prior to presentation at our hospital. He had seen many medical specialists in his home country to no avail. By the time he traveled by plane to seek an expert opinion from our medical team, he was confined to a wheelchair. At age 19, he was still a very athletic undergraduate. He developed an excruciating arthralgia associated with proximal myopathy, kyphosis, and pectus excavatum. Past history was negative for malabsorption, muscular dystrophy, tuberculosis, connective tissue disease, and glucocorticoid use. Extensive laboratory investigations were remarkable for a severe persistent refractory hypophosphatemia coupled with renal phosphate wasting associated with elevated serum alkaline phosphatase and osteoporotic-range bone mineral density with very low Z-scores as shown by dual-energy X-ray absorptiometry scan (T-score −5.5, Z-score −5.4) suggestive of a secondary cause of bone loss. Serum calcium, intact PTH, and 25-hydroxyvitamin D levels were all normal. Bone biopsy also revealed normal osteocytes and lamellar arrangement without any other diagnostic findings. Nerve conduction tests were normal while electromyography displayed small amplitude polyphasic discharges consistent with an irritable nonspecific myopathy. Despite severe muscle weakness, serum creatine phosphokinase, serum aldolase, and vastus lateralis muscle biopsy were normal. Given the negative family history, the late onset, normal dentition, and the biochemical picture of hypophosphatemic osteomalacia, the diagnosis of oncogenic osteomalacia was made and a tumor search was performed according to a diagnostic algorithm reflective of the acceptable standard of care, as described by other groups (4,5). Notably, an initial attempt with a whole body ^{18}F-FDG positron emission tomography (PET) scan from head to mid-thighs done in the patient's own country before he consulted our hospital was negative. A thorough clinical examination by a senior endocrinologist (MKSL) in the team led to the discovery of a small soft tissue mass lesion over the sole of the left foot. This was ultimately proven by ^{68}Ga-DOTA-TATE PET-computed tomography (CT) scan to be solely responsible for a high uptake "hot" spot (Fig. 1A-C). The tumor was excised en bloc with a good margin of normal tissue. Part of it was formalin fixed and paraffin embedded while the rest was snapped frozen. Elevated preoperative serum FGF-23 (378 RU/mL; normal < 180) rapidly declined to 99 RU/mL 4 h later and became undetectable 24 h postoperatively (3). This was accompanied by impressive resolution of the hypophosphatemia and rapid recovery in muscle power. The patient was self-ambulant 2 months postoperatively.

On light microscopy, there was a nodular tumor with irregular borders lying within the subcutaneous fat (Fig. 2A) composed of spindle cells arranged in fascicles with a storiform appearance in some areas (Fig. 2B). A hemangiopericytoma-like appearance of the blood vessels with branching, staghorn blood vessels were identified, but a prominent vascular network was not present. A significant population of osteoclast-like multinucleated giant cells was featured. Areas of hemorrhage with hemosiderin-laden macrophages were noted. Adipocytic component within the tumor, hyalinized to smudgy appearing matrix and grungy calcifications, were not identified on immunohistochemistry.

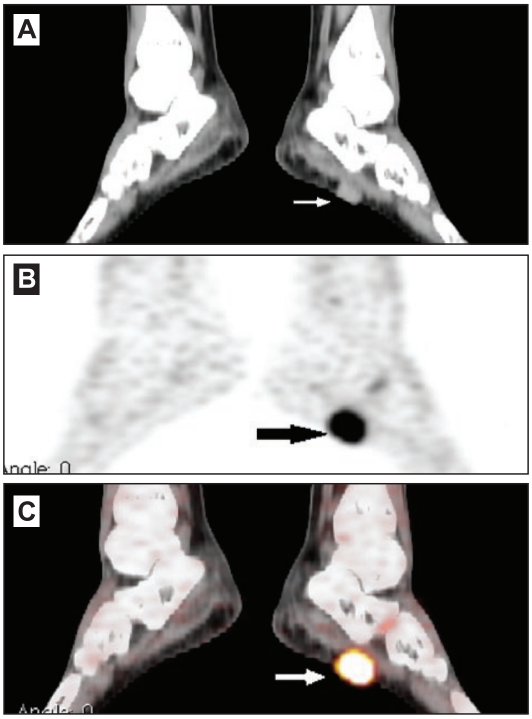

Figure 1. Sagittal section images of the sole of the left foot. Image reveals a lesion (arrowhead) on CT (**A**) corresponding to a region of intense ^{68}Ga-DOTATATE radionuclide uptake on PET scan (**B**), both of which co-localize in the fusion PET-CT image (**C**).

The spindle cells were CD163 positive (Fig. 2C); however, the multinucleated giant cells were negative for this marker. The stains for STAT6, CD34, CD31, ERG, SMA, desmin, and S-100 were negative and excluded differential diagnoses, such as vasoformative tumor (eg, hemangioma), dermatofibrosarcoma protruberans, solitary fibrous tumor, and smooth muscle tumor. Factor XIIIa staining was confined to the multinucleated giant cells (Fig. 2D). Based on these findings of CD163 and factor XIIIa expressions, fibrous histiocytoma was favored as it corroborated with the morphological findings. Thus, the histological diagnosis was judged to be more consistent with a deep benign fibrous histiocytoma than the usual mesenchymal tumor typically seen in oncogenic osteomalacia.

To better characterize the tumor ex vivo, molecular analyses were undertaken. Microarray analysis was performed to compare gene expression differences between tumor, adjacent normal tissue (labeled "adjacent") and resected overlying skin (labeled "skin"). Analysis revealed 687 significantly upregulated genes in tumor *vs* adjacent and 1837 genes in tumor *vs* skin, with 290 common genes upregulated between the 2. Similarly, there were 623 significantly downregulated genes in tumor *vs* adjacent and 1522 genes in tumor *vs* skin, with 110 common genes downregulated between the 2. Overall, there were 400 common genes in the combined up- and downregulated list, which were used for pathway analysis. The complete raw data pertaining to this microarray analysis can be found at the Gene Expression Omnibus data repository (accession no. GSE160445) (6). Subsequent pathway analysis revealed that processes, such as cell proliferation and differentiation, cell adhesion/migration, and epithelial-to-mesenchymal transition were significantly represented. In particular, Hedgehog and PTH signaling pathways in bone and cartilage development were significantly positively enriched (P-value = 4.084×10^{-4} with a false discovery rate (FDR) of 0.02275) (Table 1), which is highly relevant in the context of a soft tissue tumor that influences muscle and bone.

Importantly, microarray analysis revealed that the expression of phosphatonins, previously linked to oncogenic osteomalacia (7), were significantly upregulated in tumor tissue, when compared to adjacent tissue, with an ~360-fold increase in FGF-23, ~206-fold increase in matrix extracellular phosphoglycoprotein (MEPE), and an ~150-fold increase in secreted frizzled-related protein subtype 4 (sFRP-4) gene expression noted (Table 2). A significant increase in the expression of FGF-23 (~3700-fold) and sFRP-4 (~3400-fold) was also noted in tumor tissue, when compared to skin tissue (Table 2) and although not significant (FDR P = 0.053), the expression of MEPE was also upregulated (~8300-fold) in tumor tissue, when compared to skin tissue (Table 2). Subsequent immunoblot analyses confirmed increased levels of the phosphatonins FGF-23, MEPE, and sFRP-4 (Fig. 3) in tumor tissue, when compared to adjacent tissue. Microarray analysis further revealed increased expression of *DMP1* (a gene that encodes for dentin matrix protein-1, which is implicated in regulating bone mineralization (8), in tumor tissue, when compared to adjacent tissue (~30-fold) and skin tissue (~45-fold), although the increased expression was not significant (FDR P = 0.12 and P = 0.131 in tumor tissue *vs* adjacent and skin tissue, respectively) (Table 2). However, in contrast to the microarray data, immunoblot analysis revealed a reduction in dentin matrix protein-1 levels in tumor tissue (Fig. 3).

Interestingly, microarray analysis further revealed significantly increased expression of genes associated with osteopenia (Gremlin1; *GREM-1*) (9), bone mineralization and osteoblast differentiation (secreted phosphoprotein 1; *SPP1* [osteopontin; *OPN*] and tenascin C; *TNC*) (10, 11) and significantly reduced expression of a gene involved in bone formation (FosB proto-oncogene, AP-1 transcription factor subunit; *FOSB*) (12), in tumor tissue, when compared to both adjacent and skin tissue (Table 2). Subsequent quantitative polymerase chain reaction (qPCR) analysis was performed to confirm *GREM1* (3 transcript variants), *SPP1* (2 transcript variants), *TNC* (1 transcript variant) and *FOSB* (2 transcript variants) gene expression

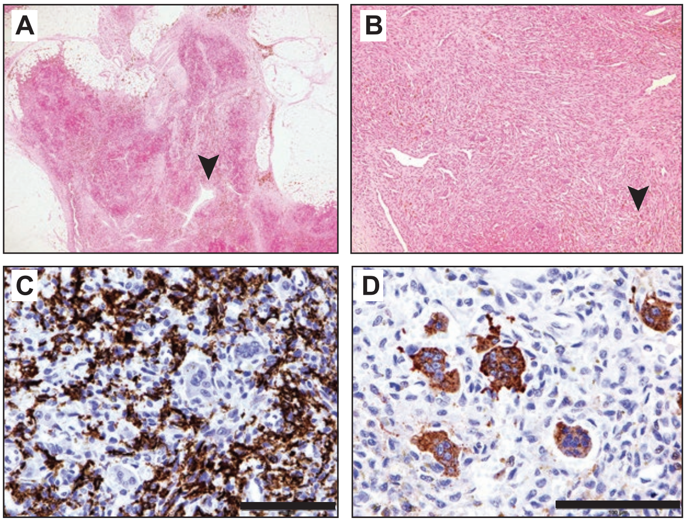

Figure 2. Images of histology and immunohistochemistry staining of tumour tissue. **(A)** Low power view revealing a partially circumscribed tumor with occasional irregular borders lying within the subcutaneous fat of the skin. Note the presence of blood vessels with staghorn appearance (indicated by arrow) and hemosiderin deposition. (H&E, magnification ×20). **(B)** Medium power view disclosing a proliferation of slender to plump spindle cells in fascicles with storiform arrangement (indicated by arrow) in some areas in association with osteoclast like multinucleated giant cells. (hematoxylin and eosin, original magnification ×100). **(C)** Decoration of spindle cells by antibody against CD163 on high power view. Note that the lack of pick up in the multinucleated giant cells (Ventana Optiview, original magnification ×600). **(D)** Factor XIIIa staining highlighting the multinucleated giant cells. (Ventana Optiview, original magnification ×400). Scale bars = 100 µm.

Table 1. Significantly enriched pathways in tumor tissue

No	Pathway	*P*-value	FDR *P*-value
1	Cell adhesion_ECM remodeling	2.76^{-07}	0.0001247
2	Cell adhesion_Chemokines and adhesion	1.06^{-05}	0.0024
3	Immune response_Antigen presentation by MHC class II	4.31^{-05}	0.006169
4	Cell adhesion_Endothelial cell contacts by non-junctional mechanisms	5.47^{-05}	0.006169
5	Cell adhesion_Integrin-mediated cell adhesion and migration	1.93^{-04}	0.01743
6	LRRK2 in neurons in Parkinson's disease	2.68^{-04}	0.02018
7	Cell adhesion_Plasmin signaling	3.57^{-04}	0.02275
8	Development_Hedgehog and PTH signaling pathways in bone and cartilage development	4.08^{-04}	0.02275
9	Cytoskeleton remodeling_Cytoskeleton remodeling	4.54^{-04}	0.02275
10	Transport_Macropinocytosis regulation by growth factors	8.59^{-04}	0.03225
11	Development_Leptin signaling via JAK/STAT and MAPK cascades	9.20^{-04}	0.03225
12	Development_Regulation of epithelial-to-mesenchymal transition (EMT)	9.34^{-04}	0.03225
13	Cell adhesion_Cadherin-mediated cell adhesion	1.07^{-03}	0.03225
14	Immune response_IL-10 signaling pathway	1.07^{-03}	0.03225
15	Development_S1P2 and S1P3 receptors in cell proliferation and differentiation	1.07^{-03}	0.03225
16	Regulation of degradation of deltaF508 CFTR in CF	1.24^{-03}	0.035
17	Development_Slit-Robo signaling	1.86^{-03}	0.04935

Table shows significantly enriched pathways (FDR *P*-value < 0.05) in tumor tissue based on identified differentially expressed genes. Common up- and downregulated genes were identified upon comparing tumor tissue to both adjacent and skin tissue. Pathway names, raw *P*-value, and FDR *P*-value are given.

changes across the tissue samples. Quantitative PCR data were normalized to both *GAPDH* (Fig. 4A) and *HPRT* (Fig. 4B), with comparable gene expression changes noted. In contrast to microarray results, the expression of *GREM-1* was reduced in tumor tissue samples, when compared to adjacent stroma tissue (Fig. 4A and B). However, consistent with microarray data, increased expression of *SPP1* and *TNC* and reduced expression of *FOSB* was confirmed in tumor tissue, when compared to adjacent and skin tissues (Fig. 4A and B).

Table 2. Selected subset of differentially expressed genes

	Tumor Tissue *vs* Adjacent Tissue			Tumor Tissue *vs* Skin Tissue		
Symbol	Fold change	*P*-value	FDR *P*-value	Fold change	*P*-value	FDR *P*-value
FGF23	361.36	0.0012	0.0425	3726.29	0.0001	0.0104
MEPE	205.88	0.0005	0.0326	8308.04	0.0055	0.053
SFRP4	155.13	0.0007	0.0354	3453.5	0.0003	0.0145
DMP1	31.13	0.0151	0.12	44.46	0.0312	0.131
GREM1	57.8	0.0009	0.0387	10.1	0.0047	0.0493
SPP1	141.81	4.75^{-05}	0.0147	4805.01	0.003	0.0403
TNC	90.5	9.13^{-05}	0.0191	215.67	0.0003	0.0149
FOSB	–37.43	0.0004	0.0305	–368.83	7.87^{-06}	0.0033

Table lists a selected subset of differentially expressed genes, identified through microarray analysis comparing (i) tumor tissue and adjacent tissue and (ii) tumor tissue *vs* skin tissue. Gene symbols, fold changes, raw *P*-value and FDR *P*-value are given for each comparison. Negative numbers reflect fold repression of gene expression.

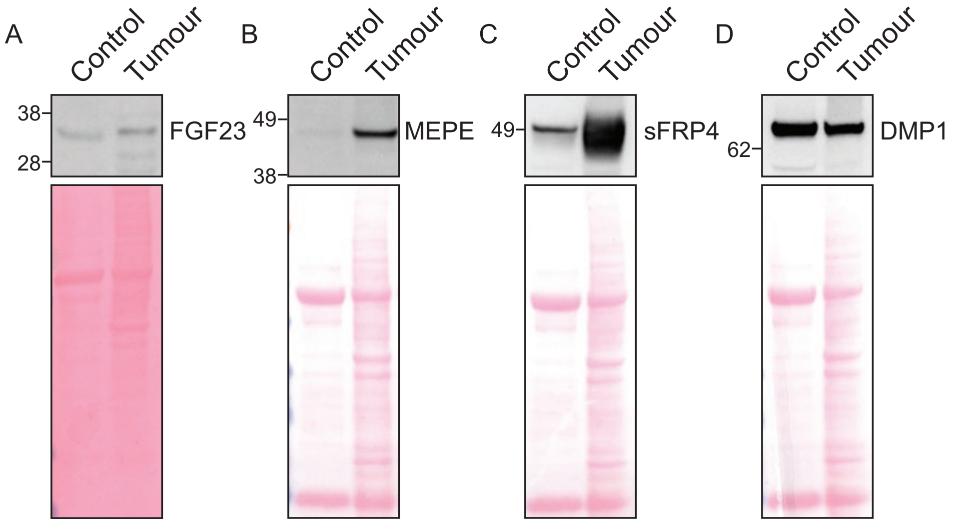

Figure 3. Immunoblot analysis. **(A)** Fibroblast growth factor subtype 23 (FGF-23), **(B)** matrix extracellular phosphoglycoprotein (MEPE), **(C)** secreted frizzled-related protein subtype 4 (sFRP4) and **(D)** Dentin matrix protein 1 (DMP1) protein levels within tumor tissue (tumor) and adjacent normal tissue (control). Ponceau S staining was performed as a loading control. The size (in KDa) of relevant molecular weight marker proteins are indicated on the left of each image.

Institutional Review Board Approval

Ethical approval for the conduct of this research on the biobanked tissue samples of this patient was formally obtained from the Institutional Review Board of the National Healthcare Group (NHG) of Singapore. The ethics code is C/2013/00206. This study was done in accordance with the principles set out in the Declaration of Helsinki.

Materials and Methods

^{68}Ga-DOTA-TATE PET-CT fusion scan

Peptide labeling with ^{68}Ga in the Department of Nuclear Medicine and Molecular Imaging, Singapore General Hospital was performed manually. In brief, 250 µg HA-DOTA-[Tyr^{3}] octreotate precursor was radiolabeled with gallium-68 eluted from ^{68}Ge/^{68}Ga generator (iThemba, South Africa). The ^{68}Ge/^{68}Ga generator was eluted with 10 mL of 0.6 N hydrochloric acid. Two milliliters of the ^{68}Ga eluent was collected into a vented preheated vial. Two milliliters of Hepes buffer (280 mg/mL) was added, followed by 250 µg of HA-dotatate. The vial was heated for 15 min at 100°C. One milliliter of Hepes buffer (1060 mg/ml) and 0.8 mL of 2 N NaOH were then added. The final product was filtered through a 0.22 µm Millex filter. Radiochemical purity was established by thin layer chromatography and the purity exceeded 90%. Whole-body ^{68}Ga HA-DOTATATE PET/CT imaging was performed using a dedicated General Electric PET/CT system (GE Discovery 690 VCT, GE Medical Systems,

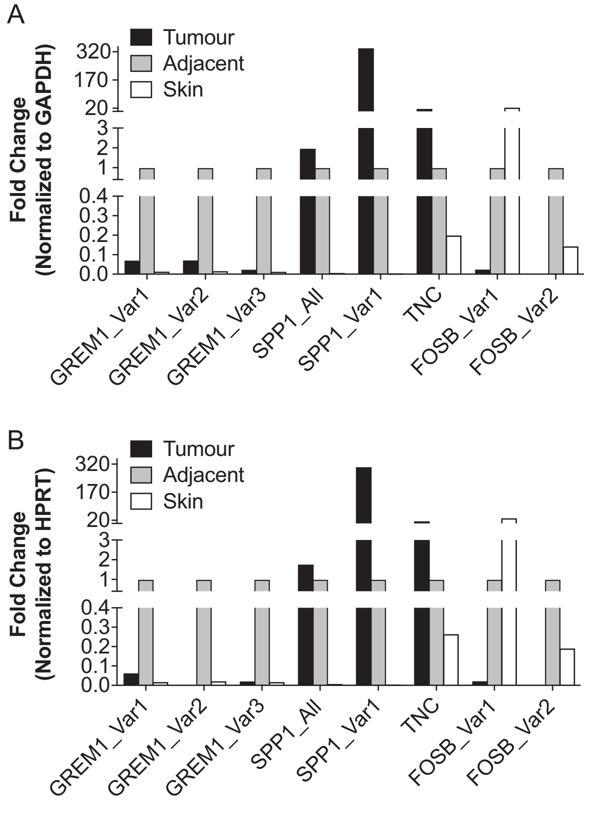

Figure 4. Graphs displaying qPCR analysis of three transcript variants of *GREM1* (Var1, Var2, and Var3), two transcript variants of *SPP1* (All and Var1), *TNC* and 2 transcript variants of *FOSB* (Var1 and Var2) in tumor tissue (Tumor), adjacent normal tissue (Adjacent) and resected overlying skin (Skin). Data are shown as fold change, relative to adjacent normal tissue, with data normalized to either **(A)** *GAPDH* or **(B)** *HPRT*.

LLC, Waukesha, WI, USA). The scan was acquired from the skull vertex to feet. Computed tomography was performed without intravenous contrast media application for the purpose of attenuation correction as follows: 100 kV; "GE smart mA dose modulation" helical thickness, 3.75 mm; table speed, 0.984 mm; rotation time, 0.8 s. Attenuation-corrected whole-body (vertex of skull to feet) scan was acquired in 3-dimensional mode (2-min emission time per bed position). Depending on body length, 16 bed positions were used with a field of view of 70 cm. For iterative reconstruction of the time of flight data, 3 iterations and 24 subsets with a filter cutoff of 7.0 were used. The patient received an intravenous injection of 203 MBq of ^{68}Ga HA-DOTATATE and the acquisition was started after an uptake time of 60 min. Multiplanar reconstruction was performed for image interpretation. Images were interpreted by an experienced nuclear medicine physician. A semiquantitative measurement of intensity of tracer uptake was performed using the maximum standardized uptake value. For maximum standardized uptake value calculations, volumes of interest of the lesion was drawn automatically and adjusted manually to lesion size, applying a commercially available software provided by the vendor of the PET/CT-scanner (GE AWS).

Histology and immunohistochemistry staining

The excision specimen from the left foot comprising skin and subcutaneous tissue was received in buffered neutral formalin. The tumor in the specimen was extensively sampled and processed for routine hematoxylin and eosin–stained sections. Five-µm sections from formalin-fixed, paraffin-embedded tissues were stained with antibodies against CD31 (Neomarker), CD34 (DAKO), ERG (Cell Marque), STAT6 (Cell Marque), Factor XIIIa (Cell Marque), CD163 (Cell Marque), desmin (DAKO), and SMA (DAKO) using the Ventana Optiview detection kit on the Roche Ventana BenchMark ULTRA slide stainer (Roche Diagnostics) after antigen retrieval, if required. For CD34, STAT6, Factor XIIIa, CD163, and desmin stains, the ULTRA cell conditioning method on the Roche Ventana BenchMark ULTRA slide stainer was used for antigen retrieval. For ERG and CD31 stains, the pressure cooker with citrate buffer at pH6 method was employed. For SMA, no antigen retrieval treatment was required.

Ribonucleic acid isolation

Tumor tissue, adjacent normal tissue and resected overlying skin tissue biopsies were stored in RNAlater (Ambion) prior to ribonucleic acid (RNA) extraction. Total RNA was isolated from each tissue using QIAzol lysis reagent (Qiagen), as per the manufacturer's instructions. The integrity of isolated RNA was evaluated using the Agilent 2100 Bioanalyzer system and the RNA 6000 Nano Kit (Agilent). All samples were stored at −80°C prior to further use.

Microarray and pathway analysis

Purified RNA was subjected to microarray analysis using the Illumina human HT-12 beadchip and in-house hybridization, quantification and analysis protocols (OCI Genomics Centre, Toronto, Canada). Microarray raw data were submitted to Gene Expression Omnibus (Accession No. GSE160445) (6). From the microarray data, 2 comparisons were made—tumor *vs* adjacent tissue and tumor *vs* skin. A 1-way analysis of variance and Benjamini-Hochberg multiple testing correction procedure were used to identify statistically significant changes in gene expression (defined as adjusted *P*-value < 0.05) using the software ArrayStudio (version 6.0) from Omicsoft. MetaCore (version 6.8, build 29806; GeneGo Inc.) was used to identify significantly enriched pathways based on the differentially expressed genes. For this purpose, the common up and down genes (significant at FDR *P*-value < 0.05) were identified from the 2 comparisons mentioned earlier. To calculate the FDR, we have used the method by Benjamini and Hochberg, as is standard in gene expression analysis studies (13).

Reverse transcription and quantitative PCR

A total of 0.250 µg of RNA was subjected to reverse transcription using the iScript complementary deoxyribonucleic acid (DNA) synthesis kit (Bio Rad Cat No: 170–8891), as per the manufacturer's protocol. Prior to qPCR analysis complementary DNA was diluted 1:10 in autoclaved MilliQ water. Quantitative PCR analysis was performed with 3 technical replicates using the SsoFast EvaGreen Supermix (Bio-Rad cat no: 7500001227) and the Bio-Rad CFX96 real-time polymerase chain reaction detection system. The qPCR conditions used were as follows: 95°C for 3 min, followed by 40 cycles of a 3-step reaction: 95°C for 10 s, 60°C for 30 s, and 72°C for 30 s. These cycles were followed by a melt curve protocol: 95°C for 10 s, followed by 65°C to 95°C in 10 s increments of 0.5°C. Gene expression fold change was calculated using the $2^{-\Delta\Delta Ct}$ method, with values normalized to *GAPDH* and *HPRT*. The sequences of the primers used in this study are *GREM1* (Var1)-F: 5'-ACT GAC AGT ATG AGC CGC AC-3', *GREM1* (Var1)-R: 5'-GCA CCT TGG GAC CCT TTC TT-3'; *GREM*1 (Var2)-F: 5'-AGA CAA GGC CCT GCA TGT G-3', *GREM1* (Var2)-R: 5'-GAA GCG GTT GAT GGT GC-3'; *GREM1* (Var3)-F: 5'-CGC GTC ACT CTC GGT CC-3', *GREM1* (Var3)-R: 5'- CAC ATG CAG GGC TCC CAC-3'; *SPP1* (Var1)-F: 5'-GGC ATC ACC TGT GCC ATA C-3', *SPP1* (Var1)-R: 5'-CTT GGA AGG GTC TGT GGG G-3'; *SPP1* (All)-F: 5'-TGT TGG AGG ATG TCT GC-3', *SPP1* (All)-R: 5'-AGT TTT CCT TGG TCG GCG TT-3'; *TNC*-F: 5'-CGG TGG ATT CTG GGA AG-3', *TNC*-R: 5'-TCC GGT TCG GCT TCT GTA AC-3'; *FOSB* (Var1)-F: 5'-GAG CTG ACC GAC CGA CTC-3', *FOSB* (Var1)-R: 5'-CAA ATC TCT CAC CTC CGC CA-3'; *FOSB* (Var2)-F: 5'-CGG TGG ATT CTG GGA AG-3', *FOSB* (Var2)-R: 5'-TCT GTC TCC GTC TCC TCT CG-3'; *GAPDH*-F: 5'-CGC TCT CTG CTC CTG TT-3', *GAPDH*-R: 5'-CCA TGG TGT CTG AGC GAT GT-3'; *HPRT*-F: 5'-TGA GGA TTT GGA AAG GGT GTT-3', and *HPRT*-R: 5'-ATG TAA TCC AGC AGG TCA GCA-3'.

Protein extraction and immunoblot analysis

Total protein was extracted from tumor tissue and control (adjacent normal tissue) using radioimmunoprecipitation assay buffer containing: 50 mM Tris HCl pH7.5, 150 mM NaCl, 1.0 mM ethylenediamine tetra-acetate pH 8.0, 1.0% NP-40, 0.1% sodium dodecylsulphate, 0.5% sodium deoxycholate, 1 mM phenylmethylsulfonyl fluoride, 25 mM sodium fluoride, 1 mM sodium orthovanadate, 1× complete protease inhibitor cocktail (Roche Diagnostics) in phosphate-buffered saline. Bradford reagent (Bio-Rad) was used to quantify protein samples. For immunoblotting, 20 µg of total protein was separated on 4% to 12% NuPAGE Bis-Tris protein gels (Invitrogen), followed by transfer to nitrocellulose membrane using the Xcell Blot Module (Invitrogen). The primary antibodies used in this report were human anti-dentin matrix protein-1 (1:200, Santa Cruz, no. sc-73633), anti-MEPE (1:400, Santa Cruz, no. sc-377035), anti-FGF-23 (1:400, Abcam, no. ab56326), anti-sFRP4 (1:1000, Abcam, no. ab154167). Secondary HRP-conjugated antibodies used in this report were antigoat (1:5000, Bio-Rad, no. 1721034), antirabbit (1:5000, Bio-Rad, no. 1706515) and antimouse (1:5000, Bio-Rad, no. 1706516). Protein bands were detected using Western Lightning Plus Chemiluminescent reagent (Perkin Elmer Life Sciences) and the ChemiDoc Imaging System (Bio-Rad). Ponceau S staining was conducted as a loading control.

Discussion

Oncogenic osteomalacia is a very rare paraneoplastic endocrinopathy with metabolic bone sequelae usually caused by benign mesenchymal tumors. In the literature, malignant tumors such as osteosarcoma and giant cell tumors have also been found to overexpress FGF-23 and resulted in oncogenic osteomalacia (1). However, our patient's paraneoplastic phosphatonin-mediated hypophosphatemia due to a deep fibrous histiocytoma is much rarer by comparison to benign mesenchymal tumors (14); an extensive search only yielded a similar case reported nearly a decade ago (15). Notably, we have also demonstrated in our case of oncogenic osteomalacia not only elevated tumor production of FGF-23, but also simultaneous tumor co-expression of the additional phosphatonins MEPE and sFRP4. Only 1 other group had previously published the involvement of these phosphatonins in oncogenic osteomalacia nearly 2 decades ago and defined their role in the biology of bone and mineral metabolism (16). It is likely that these 3 phosphatonins jointly exert synergistic phosphate wasting actions and intensify the degree of muscle weakness and deterioration of bone micro-architecture. In agreement with De Beur et al (16), we found increased tumor expression of *DMP1* messenger RNA via microarray analysis in our case of oncogenic osteomalacia. To our surprise, Western blots actually revealed reduced protein levels of DMP1 in tumor tissue relative to control adjacent tissue. Importantly, these data are consistent with previous work that suggests a role for reduced DMP1 in stimulating increased expression of FGF-23, hypophosphatemia, and osteomalacia (8,17), which is quite consistent with the increased FGF-23 and phenotype observed in this patient. It is interesting to surmise that the inverse relationship between *DMP1* messenger RNA and DMP1 protein levels noted in this study may be due to post-transcriptional regulation processes or perhaps altered protein stability. However, further work will need to be undertaken to study DMP1 gene/protein regulation in more detail in cases of oncogenic osteomalacia to determine this.

Because a normal serum phosphate is necessary for calcium phosphate homeostasis in bones for skeletal health, chronic severe hypophosphatemia can cause osteomalacia. Fortuitously, based on the microarray analysis data, we found *GREM1*, *SPP1*, and *TNC* genes to be significantly upregulated while the *FOSB* was significantly downregulated. *GREM1* (Gremlin-1) encodes for a secreted glycoprotein that antagonizes the function of bone morphogenetic proteins. Overexpression of Gremlin has been reported to lead to osteopenia (9); thus, it is interesting to surmise that elevated *GREM1* may contribute to the bone loss and osteomalacia phenotype observed in this individual. However, it is important to highlight that the increased *GREM1* expression identified by microarray analysis was not validated by subsequent qPCR and in fact, *GREM1* expression was conversely found to be elevated in adjacent normal tissue, when compared to tumor tissue by qPCR (Fig. 4). Although microarray is a valid approach to assess gene expression it is important to note that due to the intrinsic variability present in microarray data there is a potential for identification of false positives (18). This may explain the disparity in *GREM1* expression noted in the present study and further emphasizes the importance of validating microarray data using additional methodology such as qPCR. SPP1 (secreted phosphoprotein 1), otherwise called osteopontin, is a small integrin-binding ligand, N-linked glycoprotein that constitutes part of the extracellular matrix of bones and dentin (19). SPP1 has been shown to exhibit strong mineral binding properties and function to inhibit bone mineralization (10,20). Additionally, SPP1 is required for stimulating osteoclast-mediated bone resorption and as such has important roles in regulating osteoclast activity during bone remodeling (21,22). Overexpression of SPP1 has also been reported to inhibit bone mineralization in FGF-23–deficient mice and is suggested to contribute to the osteomalacia observed in these mice (23). Hence, the severe loss of bone mass encountered in this case is unlikely to be due to chronic hypophosphatemia alone. We postulate that SPP1 plays a role in contributing to the gross osteomalacia in this form of paraneoplastic metabolic bone disorder. If SPP1 is subsequently substantiated by others in future, it would constitute a novel pathway in the pathobiology of oncogenic osteomalacia. Tenascin-C, the protein product of the *TNC* gene, is a matricellular protein whose physiological function includes embryonic development, cell adhesion, cell migration, wound healing, and osteoblastic proliferation and differentiation (11,24). Notably, tenascin-C also plays a role in tissue injury, inflammation, pathological tissue remodeling and cancer invasion (25). It remains intriguing whether tenascin-C expression by this tumor contributed to patient disease manifestation or acted as a survival factor for the tumor itself. One plausible way to delineate the role of tenascin C in tumor survival as opposed to inducing oncogenic osteomalacia is to study its relative expression in similar tumors (ie, deep fibrous histiocytomas), which lack any clinical association with osteomalacia. The other remarkable finding is the significant downregulation of the *FOSB* gene, one that deserves some comment and perhaps further research. FOSB is a protein encoded by the FBJ murine osteosarcoma viral oncogene homolog B gene. FOSB heterodimerizes with DNA-binding proteins, including the Jun-related family of proteins (c-Jun, JunB, and JunD) to form the dimeric transcription factor AP-1, which has a critical role in regulating downstream gene expression in response to numerous stimuli (26). In terms of bone physiology, there is evidence to suggest that ΔFOSB, a naturally occurring truncated variant of FOSB formed through alternative splicing of the *FOSB* gene (12), has important functions in bone formation. Specifically, it has been shown that overexpression of ΔFOSB leads to significantly increased bone formation in mice (12). Thus, it is interesting to surmise that reduced expression of FOSB, as noted in this case, may be a factor contributing to osteomalacia; however, further work will need to be performed to confirm this. Nevertheless, we acknowledge that we have not measured the levels of these proteins in the circulation, and hence the previously discussed endocrine effects mediated by SPP1, TNC, and FOSB in disordered bone turnover in this patient remains speculative at best.

The fact that muscle power was rapidly restored following successful surgical resection of the tumor implied that the myologic changes are, at least in part, relatively reversible. Unlike established severe primary osteoporosis, which typically requires a much longer duration of several years before any significant reversal in bone mass and quality following appropriate therapeutic intervention, the rate of recovery in bone density upon eradication of the underlying cause in secondary osteoporosis is much more rapid (27,28). Despite very severely reduced bone density, it is thus remarkable to find our patient's postoperative dual-energy X-ray absorptiometry performed 11 months later showing dramatic improvement in bone density to a T-score of –1.8.

In summary, the strengths of our report include an in-depth analysis of the gene expression profile of a culprit oncogenic osteomalacia-inducing tumor by microarray technique along with simultaneous immunoblot evidence of protein expression; we also highlight the plausible role of newer factors like SPP1, TNC, and FosB for the first time and elaborated on the pathway analysis. We acknowledge some weaknesses, one of which is the unavailability of a similar tumor tissue without osteomalacia as a control, which could then provide more insightful analysis and interpretation for the differentially expressed genes beyond what we can surmise by comparison against adjacent nontumoral tissue. Also, while we have found upregulation of SPP1 and TNC and downregulation of FOSB in the tumor, we have not assayed the plasma for these proteins. Thus, we have not confirmed that such proteins are circulating and exert endocrine actions on the skeleton per se. However, given that these proteins play a role in the molecular pathways of bone turnover, it would be important for more research to be done to ascertain their role in bone biology and the pathogenesis of oncogenic osteomalacia.

Finally, a note should be emphasized about how standard-field ^{18}F-FDG-PET imaging can totally miss the culprit tumors causing oncogenic osteomalacia (29,30). Our case illustrates this pitfall very elegantly and reiterates the need for clinicians to be especially thorough in the physical examination of patients being worked up for muscle weakness associated with skeletal disorders and for nuclear physicians to ensure that the PET imaging field actually covers the whole body in those suspected to suffer from this rare disorder.

Acknowledgments

We thank the patient for kindly consenting to his case being submitted for publication in a peer-reviewed journal. We wish to thank Prof. Hiok Hee Chng and Dr. Laniyati Hamijoyo for referring the patient. We are also gratefully acknowledge Dr. Isuru Wijerupage Wijesoma, for his contributions to data acquisition, specifically relating to undertaking quantitative polymerase chain reaction analysis and validation of identified microarray target genes.

Financial Support: This study was funded by the Agency for Science, Technology and Research (A*STAR), Singapore.

Additional Information

Correspondence and Reprint Requests: Dr. Craig McFarlane, Department of Molecular and Cell Biology, College of Public Health, Medical and Veterinary Sciences, 1 James Cook Drive, Townsville, QLD 4811, Australia. Email: craig.mcfarlane@jcu.edu.au.

Disclosure Summary: The authors declare no conflicts of interest.

Data Availability: Some or all data generated or analyzed during this study are included in this published article or in the data repositories listed in references.

References

1. Folpe AL, Fanburg-Smith JC, Billings SD, et al. Most osteomalacia-associated mesenchymal tumors are a single histopathologic entity: an analysis of 32 cases and a comprehensive review of the literature. *Am J Surg Pathol.* 2004;**28**(1):1-30.
2. Lin HA, Shih SR, Tseng YT, et al. Ovarian cancer-related hypophosphatemic osteomalacia: a case report. *J Clin Endocrinol Metab.* 2014;**99**(12):4403-4407.
3. Leow MK, Hamijoyo L, Liew H, et al. Oncogenic osteomalacia presenting as a crippling illness in a young man. *Lancet.* 2014;**384**(9949):1236.
4. Florenzano P, Gafni RI, Collins MT. Tumor-induced osteomalacia. *Bone Rep.* 2017;**7**:90-97.
5. Minisola S, Peacock M, Fukumoto S, et al. Tumour-induced osteomalacia. *Nat Rev Dis Primers.* 2017;**3**:17044.
6. Leow MK, Dogra S, Ge X, et al. Data from: paraneoplastic secretion of multiple phosphatonins from a deep fibrous histiocytoma causing oncogenic osteomalacia. 2020. *Gene Expression Omnibus (GEO).* Deposited 30 October 2020. ProMED-mail website. https://www.ncbi.nlm.nih.gov/geo/query/acc.cgi?acc=GSE160445. Last updated October 31, 2020.
7. Farrow EG, White KE. Tumor-induced osteomalacia. *Expert Rev Endocrinol Metab.* 2009;**4**(5):435-442.
8. Feng JQ, Ward LM, Liu S, et al. Loss of DMP1 causes rickets and osteomalacia and identifies a role for osteocytes in mineral metabolism. *Nat Genet.* 2006;**38**(11):1310-1315.
9. Gazzerro E, Pereira RC, Jorgetti V, Olson S, Economides AN, Canalis E. Skeletal overexpression of gremlin impairs bone formation and causes osteopenia. *Endocrinology.* 2005;**146**(2):655-665.
10. Addison WN, Azari F, Sørensen ES, Kaartinen MT, McKee MD. Pyrophosphate inhibits mineralization of osteoblast cultures by binding to mineral, up-regulating osteopontin, and inhibiting alkaline phosphatase activity. *J Biol Chem.* 2007;**282**(21):15872-15883.
11. Mackie EJ, Ramsey S. Modulation of osteoblast behaviour by tenascin. *J Cell Sci.* 1996;**109 (Pt 6)**:1597-1604.
12. Sabatakos G, Sims NA, Chen J, et al. Overexpression of DeltaFosB transcription factor(s) increases bone formation and inhibits adipogenesis. *Nat Med.* 2000;**6**(9):985-990.
13. Benjamini Y, Hochberg Y. Controlling the false discovery rate: a practical and powerful approach to multiple testing. *J R Stat Soc Series B Stat Methodol.* 1995;**57**(1):289-300.
14. Unni KK, Inwards CY. *Dahlin's Bone Tumors.* 6th ed. Philadelphia, PA: Wolters Kluwer, Lippincott Williams & Wilkins; 2009.
15. Jagtap VS, Sarathi V, Lila AR, et al. Tumor-induced osteomalacia: a single center experience. *Endocr Pract.* 2011;**17**(2):177-184.
16. De Beur SM, Finnegan RB, Vassiliadis J, et al. Tumors associated with oncogenic osteomalacia express genes important in bone and mineral metabolism. *J Bone Miner Res.* 2002;**17**(6):1102-1110.

17. Liu S, Zhou J, Tang W, Menard R, Feng JQ, Quarles LD. Pathogenic role of Fgf23 in Dmp1-null mice. *Am J Physiol Endocrinol Metab.* 2008;**295**(2):E254-E261.
18. Jaluria P, Konstantopoulos K, Betenbaugh M, Shiloach J. A perspective on microarrays: current applications, pitfalls, and potential uses. *Microb Cell Fact.* 2007;**6**:4.
19. Fisher LW, Fedarko NS. Six genes expressed in bones and teeth encode the current members of the SIBLING family of proteins. *Connect Tissue Res.* 2003;**44**(Suppl 1):33-40.
20. Sodek J, Ganss B, McKee MD. Osteopontin. *Crit Rev Oral Biol Med.* 2000;**11**(3):279-303.
21. Chellaiah MA, Kizer N, Biswas R, et al. Osteopontin deficiency produces osteoclast dysfunction due to reduced CD44 surface expression. *Mol Biol Cell.* 2003;**14**(1):173-189.
22. Tani-Ishii N, Tsunoda A, Umemoto T. Osteopontin antisense deoxyoligonucleotides inhibit bone resorption by mouse osteoclasts in vitro. *J Periodontal Res.* 1997;**32**(6):480-486.
23. Yuan Q, Jiang Y, Zhao X, et al. Increased osteopontin contributes to inhibition of bone mineralization in FGF23-deficient mice. *J Bone Miner Res.* 2014;**29**(3):693-704.
24. Giblin SP, Midwood KS. Tenascin-C: form versus function. *Cell Adh Migr.* 2015;**9**(1-2):48-82.
25. Midwood KS, Orend G. The role of tenascin-C in tissue injury and tumorigenesis. *J Cell Commun Signal.* 2009;**3**(3-4):287-310.
26. Wagner EF, Eferl R. Fos/AP-1 proteins in bone and the immune system. *Immunol Rev.* 2005;**208**:126-140.
27. Bhambri R, Naik V, Malhotra N, et al. Changes in bone mineral density following treatment of osteomalacia. *J Clin Densitom.* 2006;**9**(1):120-127.
28. Nordenström E, Westerdahl J, Bergenfelz A. Recovery of bone mineral density in 126 patients after surgery for primary hyperparathyroidism. *World J Surg.* 2004;**28**(5):502-507.
29. Chong WH, Yavuz S, Patel SM, Chen CC, Collins MT. The importance of whole body imaging in tumor-induced osteomalacia. *J Clin Endocrinol Metab.* 2011;**96**(12):3599-3600.
30. Kaneuchi Y, Hakozaki M, Yamada H, Hasegawa O, Tajino T, Konno S. Missed causative tumors in diagnosing tumor-induced osteomalacia with (18)F-FDG PET/CT: a potential pitfall of standard-field imaging. *Hell J Nucl Med.* 2016;**19**(1):46-48.